Scattering properties of the three-dimensional topological insulator Sb$_2$Te$_3$: Coexistence of topologically trivial and nontrivial surface states with opposite spin-momentum helicity

P. Sessi,[1,*] O. Storz,[1] T. Bathon,[1] S. Wilfert,[1] K. A. Kokh,[2,3,4] O. E. Tereshchenko,[3,4,5] G. Bihlmayer,[6] and M. Bode[1,7]

[1]*Physikalisches Institut, Experimentelle Physik II, Universität Würzburg, Am Hubland, 97074 Würzburg, Germany*
[2]*V.S. Sobolev Institute of Geology and Mineralogy, Siberian Branch, Russian Academy of Sciences, 630090 Novosibirsk, Russia*
[3]*Novosibirsk State University, 630090 Novosibirsk, Russia*
[4]*Saint-Petersburg State University, 198504 Saint-Petersburg, Russia*
[5]*A.V. Rzanov Institute of Semiconductor Physics, Siberian Branch, Russian Academy of Sciences, 630090 Novosibirsk, Russia*
[6]*Peter Grünberg Institut and Institute for Advanced Simulation, Forschungszentrum Jülich and JARA, 52428 Jülich, Germany*
[7]*Wilhelm Conrad Röntgen-Center for Complex Material Systems (RCCM), Universität Würzburg, Am Hubland, 97074 Würzburg, Germany*

The binary chalcogenides Bi$_2$Te$_3$ and Bi$_2$Se$_3$ are the most widely studied topological insulators. Although the quantum anomalous Hall effect has recently been observed in magnetically doped Sb$_2$Te$_3$, this compound has been studied to a much lesser extent. Here, by using energy-resolved quasiparticle interference mapping, we investigate the scattering events of pristine Sb$_2$Te$_3$ surfaces. We find that, in addition to the Dirac fermions, another strongly spin-polarized surface resonance emerges at higher energies in the unoccupied electronic states. Although the two surface states are of different origin, i.e., topologically protected and trivial, respectively, both show strongly directional scattering properties and absence of backscattering. A comparison with *ab initio* calculations demonstrates that this is a direct consequence of their spin-momentum–locked spin texture which is found to exhibit an opposite rotational sense for the trivial state and the Dirac state.

I. INTRODUCTION

The discovery of topological insulators (TIs) [1–3] led to intense research efforts towards the potential utilization of these materials in spintronic, magnetoelectric, or quantum computation devices [4–7]. In particular, the existence of a linearly dispersing, gapless surface state is of enormous interest, because—contrary to the trivial surface states usually found at surfaces of metals and semiconductors—it cannot be destroyed by the presence of defects and adsorbates as long as time-reversal symmetry is preserved [8–14]. The strong spin-orbit coupling inherent to these systems perpendicularly locks the spin to the momentum, creates a helical spin texture which forbids backscattering [15,16], and results in spin currents that are intrinsically tied to charge currents [1].

Among the three-dimensional (3D) TIs, the binary chalcogenides Bi$_2$Te$_3$ [3] and Bi$_2$Se$_3$ [17] represent the most widely studied compounds. In contrast, the electronic properties of Sb$_2$Te$_3$ [18] which belongs to the same material class have been studied to a much lesser extent. This deficiency can directly be linked to the intrinsic strong p doping characterizing the compound, which leads to a Dirac point that lies well above the Fermi level [19–21]. As a result relevant parts of the surface electronic band structure are inaccessible to angle-resolved photoemission spectroscopy (ARPES), a technique that played a key role towards the identification and study of topologically nontrivial states of matter.

Another technique frequently applied to TIs, which gives access to the scattering properties of surfaces not only for occupied states below but also for empty electronic states above the Fermi level, is quasiparticle interference (QPI) imaged with a scanning tunneling microscope (STM) [9,14–16,22]. However, the observation of QPI signals in TIs depends on the deformation of the Dirac cone which is described by the so-called warping term [23]. This contribution to the Hamilton operator leads to an effective nesting of equipotential surfaces and to the development of out-of-plane spin polarization components, which both result in new scattering channels and a higher QPI signal strength. Unfortunately, the warping term of Sb$_2$Te$_3$ is very weak as compared to Bi$_2$Te$_3$ [16,22,24]. This together with the above-mentioned p doping, which requires one to work at energies far above the Fermi level and results in strongly reduced lifetimes and rapidly damped standing wave patterns, makes scattering experiments on Sb$_2$Te$_3$ highly challenging.

This deficiency is the more annoying as the quantum anomalous Hall effect has recently been observed in magnetically doped Sb$_2$Te$_3$ [25,26]. Therefore, a comparison of the scattering properties with pristine Sb$_2$Te$_3$ would be highly interesting to identify the correlation between dissipationless quantized transport and the onset of ferromagnetism in a topologically nontrivial material. Here, we close this gap by QPI of p-doped Sb$_2$Te$_3$ which contains defects that effectively scatter the surface state. In addition to the linearly dispersing spin-momentum–locked Dirac states, our data evidence the existence of another surface-related electronic feature with strongly directional scattering properties. A comparison with *ab initio* calculations reveals that the latter originates from a trivial surface resonance which also possesses a helical spin texture suppressing backscattering. Interestingly, the helical spin texture of the Dirac state and the trivial surface resonance are opposite. This unique feature may allow for the independent tuning of spin and charge currents, for example by tuning the potentials by means of gating.

_____
*Corresponding author: sessi@physik.uni-wuerzburg.de

II. EXPERIMENTAL PROCEDURES

The Sb_2Te_3 single crystal was grown by the modified vertical Bridgman method with rotating heat field [27]. Stoichiometric amounts of Sb and Te were loaded to a carbon-coated quartz ampoule. After evacuation to 10^{-4} torr the ampoule translation rate and axial temperature gradient were set to 10 mm/day and $\approx 15°/cm$, respectively. Single crystals of about 10 mm in diameter and 30 mm in length were obtained as shown in Fig. 1(a).

After growth, crystals have been cut in sizes suitable for STM experiments, cleaved at room temperature in ultrahigh vacuum (UHV), and immediately inserted into a cryogenic STM. Because of the Sb_2Te_3 structure depicted in Fig. 1(b), which consists of quintuple layers that are weakly bound by van der Waals forces, the surface is always Te terminated. Spectroscopic data have been obtained by low-temperature scanning tunneling microscopy at $T = 1.5 \dots 4.8$ K under ultrahigh vacuum conditions ($p \leqslant 10^{-10}$ mbar) using the lock-in technique ($f = 793$ Hz) with a modulation voltage $U_{mod} = 10 \dots 20$ meV. Unless otherwise stated experiments were performed at zero magnetic field. While maps of the differential conductance dI/dU have been acquired simultaneously with topographic images in the constant-current mode, scanning tunneling spectroscopy (STS) curves are measured by ramping the bias voltage after deactivation of the feedback loop, i.e., at constant tip-sample separation. In accordance with the C_{3v} symmetry of the cleaved surface, Fourier-transformed QPI data have been sixfold symmetrized.

III. RESULTS AND DISCUSSION

Figure 1(c) shows a topographic image of the Sb_2Te_3 surface with defects typical for binary chalcogenides [28]. To our experience the existence of the defect type indicated by an arrow, which probably corresponds to a Te surface vacancy, is crucial for the formation of a QPI pattern. We speculate that this may be related to the fact that only this defect exhibits a potential that sufficiently overlaps with the wave function of the topological surface state. The electronic structure is investigated by analyzing the local density of states as probed by STS. The bottom curve of Fig. 1(d) shows a typical STS spectrum obtained on pristine Sb_2Te_3 by positioning the tip away from defects (blue line). The minimum corresponds to the position of the Dirac point [18,28] which is found at about 170 meV above the Fermi level, i.e., in the empty electronic states, confirming the intrinsic *p* doping characterizing the material [19]. This assignment is also corroborated by the position of the zeroth-order Landau level measured at a magnetic field $B = 10$ T (red line).

To investigate the scattering properties of Sb_2Te_3, we performed energy-dependent QPI experiments. QPI mapping makes use of the standing-wave pattern generated by elastic scattering of electronic states at surface defects and is known as a powerful method to study scattering mechanisms. While originally applied to noble metal surfaces [29], its use has been recently extended to investigate nondegenerate spin-polarized bands, e.g., on surfaces with strong contributions from spin-orbit coupling [30,31] and topological insulators [9,14–16,22]. Fourier transformation (FT) translates real-space information
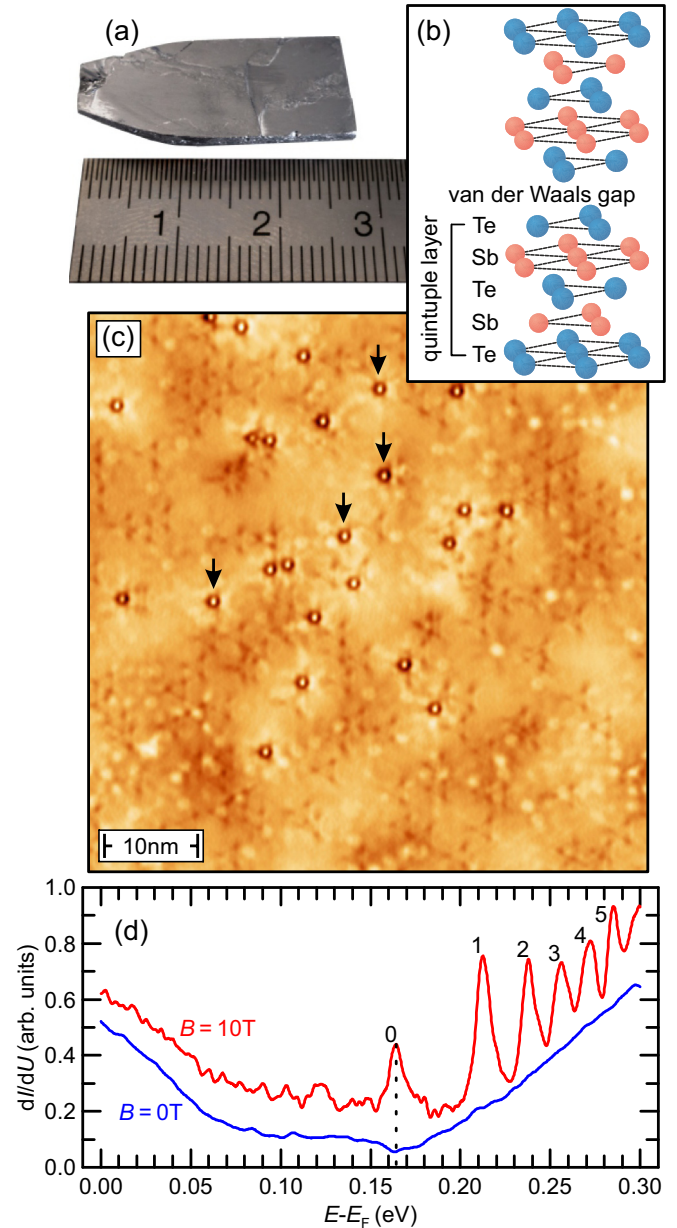

FIG. 1. (a) Photographic image of an as-grown Sb_2Te_3 single crystal after longitudinal cleavage. (b) Sb_2Te_3 crystal structure, consisting of alternating layers of Sb and Te up to the formation of a quintuple layer which is weakly bound to the next one by van der Waals forces. (c) Topographic image of the Sb_2Te_3 surface (scan parameters: $I = 50$ pA, $U = 0.5$ V). Arrows indicate the type of defects responsible for the formation of QPI patterns. (d) STS data taken on Sb_2Te_3 with (red line) and without (blue) magnetic field [set point parameters: $I = 300$ pA, $U = 0.35$ V (B=10 T); I=100 pA, $U = 0.3$ V ($B = 0$ T)]. In high magnetic fields we observe peaks representing Landau levels whose indices are indicated by numbers.

into reciprocal space, thereby providing a convenient way to visualize scattering vectors, which correspond to points of a constant energy cut (CEC) connected by nesting vectors [32].

The shape of equipotential surfaces of TIs and the spin texture are both strongly energy dependent. In Sb_2Te_3, similar to other TIs hosting a single Dirac cone centered around the $\overline{\Gamma}$
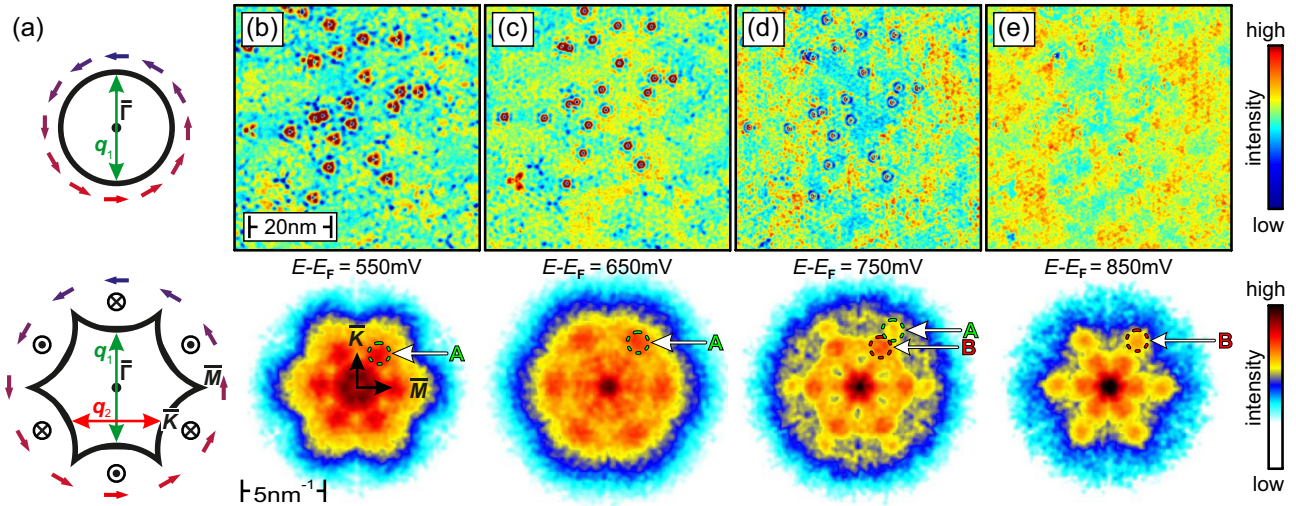
FIG. 2. (a) Schematic presentation of the equipotential surface (black), the in-plane spin polarization (blue/red arrows), and potential scattering vectors of a TI close to the Dirac point (upper panel) and at an energy closer to the bulk conduction band (bottom). Scattering vectors are indicated by $\mathbf{q}_1$ and $\mathbf{q}_2$. The former is forbidden by time-reversal symmetry. (b)–(e) dI/dU maps (upper panel) with corresponding sixfold-symmetrized FT (lower) at selected representative energies obtained over the area displayed in Fig. 1(c) (tunneling current $I = 50$ pA). Two features labeled A and B, both located in $\overline{\Gamma M}$ directions, are visible.

point of the surface Brillouin zone, one finds circular CECs at energies close to the Dirac point supporting only one nesting vector, i.e., backscattering ($\mathbf{q}_1$). As schematically represented by red/blue arrows in the upper panel of Fig. 2(a), however, the spin polarization in this energy range is perpendicularly locked to the crystal momentum k and completely in-plane. In this case backscattering is forbidden by time-reversal symmetry, which explains the absence of any scattering channel close to the Dirac point.

In contrast, at higher energies the introduction of the warping term progressively deforms the circular CEC, eventually giving rise to a snowflakelike shape, as shown in the lower panel of Fig. 2(a). At the same time the warping leads to an increasing out-of-plane modulation of the spin polarization. Although backscattering remains forbidden, it is well known from both theoretical [23] and experimental [15,16,24] investigations that the warping term opens new scattering channels along the $\overline{\Gamma M}$ direction by connecting next-nearest-neighbor concavely warped sides that are centered at the $\overline{K}$ point of the hexagram [schematically represented by the red arrow labeled $\mathbf{q}_2$ in Fig. 2(a), lower panel]. This scattering channel can be experimentally visualized by QPI. For example, Fig. 2(b) shows the dI/dU map (upper panel) and the corresponding FT (lower panel) at an energy $E = 550$ meV above the Fermi level. The FT exhibits six distinct maxima that represent $\mathbf{q}_2$ (one of which is labeled A). With increasing energy it progressively moves away from the center of the FT, thereby reflecting the band dispersion relation of the Dirac cone [Fig. 2(c)].

Careful inspection of the FT of dI/dU maps taken at higher energy reveals the emergence of another scattering channel not related to the topological surface state. This scattering channel, which is labeled B in Fig. 2(d), becomes detectable at about 750 meV above the Fermi level. It also shows a well-defined directionality with maxima pointing along the $\overline{\Gamma M}$ direction. Since its length is shorter than $\mathbf{q}_2$ we can safely

exclude an additional scattering channel involving topological states. While it initially coexists with $\mathbf{q}_2$, the new scattering channel completely dominates the FT-QPI signal at higher energies, as shown in Fig. 2(e) at $E = 850$ meV.

To identify the electronic states that lead to the appearance of this additional scattering channel on pristine Sb_2Te_3 we have quantitatively analyzed a larger series of FT-QPI maps that is only partially presented in Figs. 2(b)–2(e). The result is shown in Fig. 3(a). The linear dispersion relation of signal A (green dots) that represents the topological state is clearly visible. A fit to the data provides a Dirac point at $E_D = (202 \pm 17)$ meV above the Fermi level. This value is slightly higher than the one obtained from the STS data presented in Fig. 1(d), a deviation we attribute to the warping term, which introduces a subtle deviation from a linear dispersion relation also visible in the calculations. The slope of the linear dispersion gives a Fermi velocity $v_F = (4.3 \pm 0.2) \times 10^5$ ms^{-1}, in reasonable agreement with previous reports on binary chalcogenides [14,18,33]. In contrast, scattering channel B (red dots) appears in a narrow energy and crystal momentum range around $E - E_F = 800$ meV and $k_{\mathrm{exp}} = 1.3$ nm^{-1} only and cannot be reasonably fit. Correspondingly, the red line serves as a guide to the eye only.

These experimental data have been compared with *ab initio* density functional theory (DFT) calculations (obtained as described in Ref. [33]). We would like to emphasize that DFT calculations are here performed for ideal crystals and, therefore, always result in a Fermi level positioned at or near the valence band maximum (VBM) which is close to the Dirac point (DP) here. For this reason the experimentally observed doping-induced shift of the chemical potential cannot be simulated in DFT. Any comparison between the experiment and theory must be performed on a relative level, i.e., by comparing the position of electronic bands with respect to certain reference points. In our experiments the Fermi level is unambiguously defined by the zero-bias condition in STS
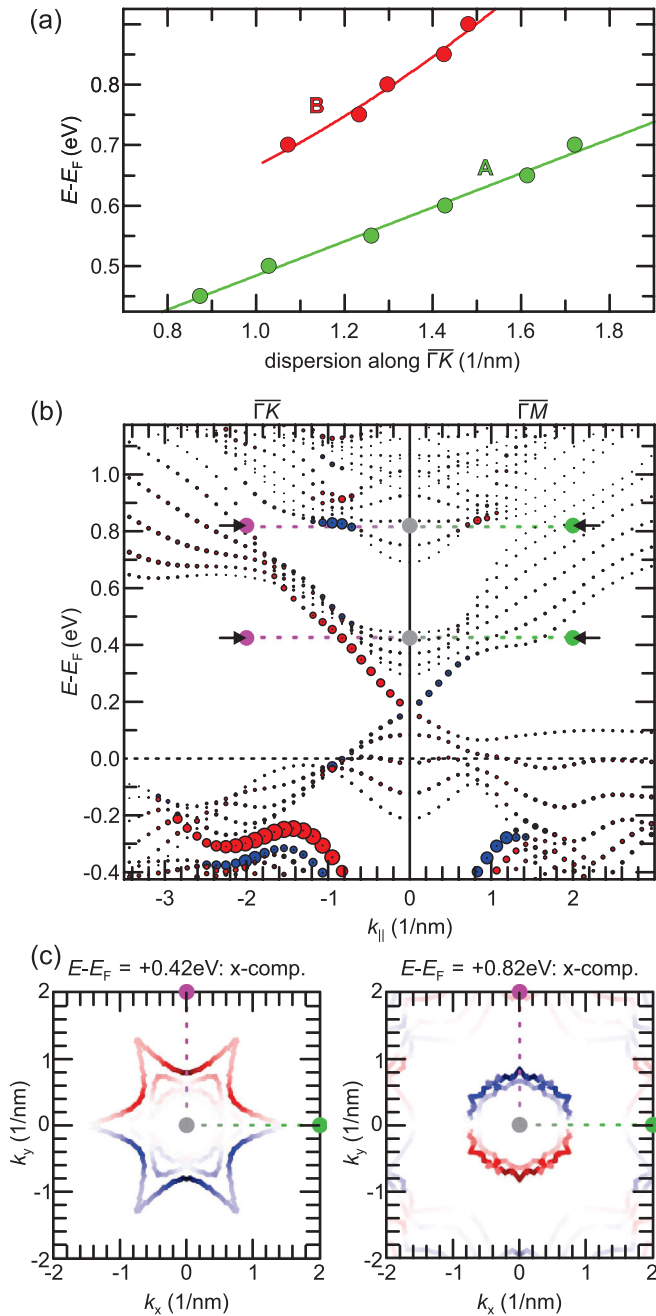
FIG. 3. (a) Experimentally determined energy dispersion relation of features A and B [cf. Figs. 2(b)–2(e)] along the $\overline{\Gamma M}$ direction. Data points show the position of maximum FT-QPI pattern intensity measured along the high symmetry directions at different energies. (b) Theoretical band structure of the Sb_2Te_3 surface. Note that the Dirac point has been shifted to the experimentally determined value to account for the doping-induced modification of the chemical potential (see the main text for details). In addition to the Dirac cone another feature with an electronlike dispersion and an onset energy of about 0.7 eV above the Fermi level can be recognized. (c) Constant-energy cuts taken at the energies indicated by black arrows in (b), i.e., 0.42 and 0.82 eV above E_F. To better relate the dispersion relation in (b) to the constant-energy cuts of (c), pink, gray, and green points are used to mark corresponding positions in the Brillouin zone along the $\overline{\Gamma K}$ direction, at the $\overline{\Gamma}$ point, and along the $\overline{\Gamma M}$ direction, respectively. Note that the two states exhibit an opposite spin polarization.

($U = 0$ V). Furthermore, the energetic position of the Dirac point relative to the Fermi level can be determined with an accuracy we estimate to about ± 10 meV. Therefore, we have chosen to shift the theoretical Dirac point energy to the experimental value, i.e., $+170$ meV [cf. Fig. 1(d)].

The band structure obtained from DFT is reported in Fig. 3(b). In good agreement with the experimental data presented in Fig. 3(a), DFT evidences the existence of an additional surface resonance with a charge density centered around $E - E_F = 800$ meV, but at a slightly lower value of the crystal momentum, $k_{theo} \approx 1.0$ nm^{-1}. To shed light on the strongly directional character of the scattering events involved from this band, its spin texture has been calculated and compared with the topological state. Results for the spin polarization component along the x direction is reported in Fig. 3(c). Interestingly, the two electronic states under discussion here, which are energetically located at around 0.42 and 0.82 eV above the Fermi level, exhibit opposite spin helicities. Furthermore, a detailed analysis of the other directional components of the spin polarization (not shown here) reveals a helical texture with significant out-of-plane components. This is expected for the warped Dirac cone, but it is also observed for the higher lying state.

As an alternative explanation for the second scattering channel one might also consider two-dimensional quantum well states (QWS) that have been found to coexist with topological states on surfaces of various n-doped TIs [34–36]. For example, Rashba-split QWS have been reported for potassium-doped Bi_2Se_3 [35]. The strong negative charge transfer from the alkali metal to the TI leads to a substantial downwards bending of the conduction band minimum and results in the formation of a near-surface electrostatic potential well which hosts states quantized in the z direction. Due to strong spin-orbit interaction the two-dimensional subbands are Rashba split. Circular dichroism experiments indicate a helical texture of both the orbital as well as the spin angular momentum [35]. Similar observations have also been reported for other TIs, such as Bi_2Se_3 exposed to the residual gas of an UHV system [34] or pristine $Bi_{2-x}Fe_xSe_3$ [36].

A comparison with the latter example, Ref. [36], is particularly well suited to discuss whether the second scattering channel observed on Sb_2Te_3 might also be explained by a QWS. In both cases maxima in the FT data appear along the $\overline{\Gamma M}$ direction at energies well above the Dirac point (about 0.7 eV). However, as shown in Figs. 3(a) and 3(b) of Ref. [36], the QWS detected on $Bi_{2-x}Fe_xSe_3$ disperses almost parallel to the topological surface state with an energy offset of about 0.1 eV only, i.e., in close proximity to the conduction band minimum. In contrast, the features observed here are energetically located about $0.2 \ldots 0.3$ eV above the topological state. This energy separation even exceeds the band gap of Sb_2Te_3 which is of the order of 0.1 eV only [37]. Such a strong band bending is completely unexpected for the sample studied here, i.e., freshly cleaved, pristine Sb_2Te_3. As pointed out by Yee *et al.* in Ref. [36] the band bending in $Bi_{2-x}Fe_xSe_3$ is probably caused by Fe interstitials located in the van der Waals (vdW) gap between the first and the second quintuple layer. Although it could not be decided which of the two mechanisms proposed—Fe ionization resulting in electron donation or physical expansion of the vdW gap—leads to the formation
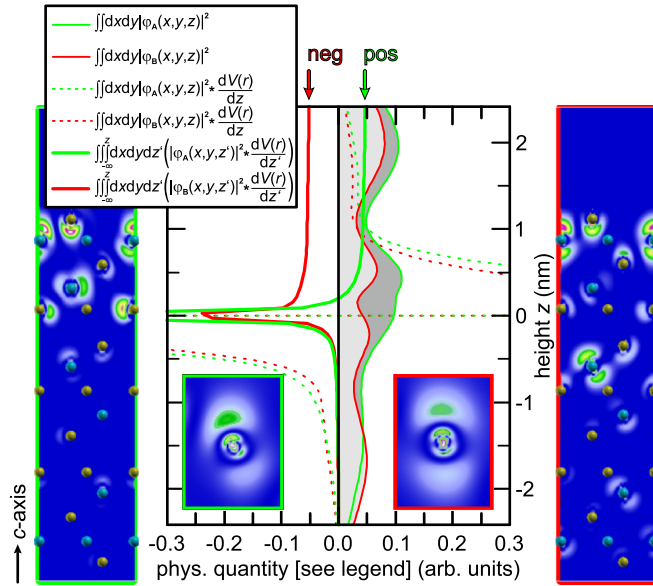
FIG. 4. Charge density plots in the $y-z$ plane of the surface states located at a k point at 1/nm in the $\overline{\Gamma K}$ direction [$E - E_F = 0.42$ eV (left panel) and 0.82 eV (right panel)]. Close-up views of the states are shown in the central panel as insets (framed green and red for the lower and higher lying electronic states, respectively). In-plane averaged charge densities ($\iint dx\, dy |\phi(x,y,z)|^2$ around the subsurface Sb atom at $z = 0$) are plotted as green and red lines in the middle panel. Moreover, the product of charge density with the derivative of a $1/|r|$ potential (dotted lines) and the integral of this product in the z direction as a function of the integration region $[-\infty, z]$ are shown. Note that sign of the latter quantity converges for large z to a positive value for the lower lying topological surface state but to a negative value for the surface resonance, giving rise to the opposite rotational sense of their spin textures.

of QWS, any significant role of tip-induced band bending could safely be excluded since it acts in the wrong direction [36]. Given the low doping concentration present in our Sb$_2$Te$_3$ crystals and the fact that the samples are kept within the cryostat at extremely low background pressure (samples typically remain unchanged over time spans of several days to weeks) we expect that, if there is any band bending present at the surface at all, it will be much smaller than what is required to explain the second scattering channel by a QWS.

To understand this surprising result of a second surface-related electronic band with opposite spin helicity we analyze the charge density in more detail, following the model of Nagano *et al.* [38]. This model unfolded that the major effect of spin-orbit coupling, which determines the spin orientation,

originates from a region close to the nucleus where the potential gradient $V(r)$ is strongest [39]. The charge density plots shown in Fig. 4 reveal that both states are predominantly localized at subsurface Sb atoms and exhibit p_z character. In spite of their similar shape, the strength of the spin-orbit coupling and the resulting spin polarization of both electronic features is found to sensitively depend on subtle variations of the exact spatial distribution of the charge density. If the state is located on average a bit above the position of the heavy Sb nucleus (i.e., shifted to positive z direction) it will be influenced by regions where $\partial_z V$ is positive, giving rise to an effective electric field acting on the state. Due to the $\boldsymbol{\sigma} \cdot (\mathbf{k} \times \boldsymbol{\nabla} V)$ term of the spin-orbit coupling, this favors one particular spin direction for a given $\mathbf{k}$ vector leading to a certain helicity of the spin texture. If the state is shifted a bit in the negative z direction, however, the other spin direction (and helicity) will be favored. In the middle panel of Fig. 4, the charge densities of the states at 0.42 and 0.82 eV, both in-plane averaged around the subsurface Bi atoms, are shown as thin black and red lines, respectively. It appears that the state at 0.42 eV is a bit more displaced towards the vacuum. To quantify the effect, we multiply the charge density with the z derivative of an atomic $(1/|r|)$ potential and integrate the product (dotted line in the middle panel of Fig. 4) in the z direction. Indeed, the integrals (thick full lines) converge to values of opposite sign for large z, thereby confirming our hypothesis that spin-orbit coupling arising from this Sb atom induces opposite spin orientations of the two states.

IV. SUMMARY

In conclusion, we have investigated the scattering properties of the three-dimensional topological insulator Sb$_2$Te$_3$. While no scattering events occur close to the Dirac point, scattering vectors connecting next-nearest-neighbor concavely warped sides of the hexagram-shaped constant energy cuts appear as soon as the warping term introduces a substantial out-of-plane spin polarization. A new surface-related electronic band with strongly directional scattering channels has been revealed at higher energy. Although its nature is not topological, it shows a well-defined spin texture, with a spin-momentum locking opposite to the Dirac fermion.

[1] M. König, S. Wiedmann, C. Brüne, A. Roth, H. Buhmann, L. W. Molenkamp, X.-L. Qi, and S.-C. Zhang, Science **318**, 766 (2007).

[2] D. Hsieh, D. Qian, L. Wray, Y. Xia, Y. S. Hor, R. J. Cava, and M. Z. Hasan, Nature (London) **452**, 970 (2008).

[3] Y. L. Chen, J. G. Analytis, J.-H. Chu, Z. K. Liu, S.-K. Mo, X. L. Qi, H. J. Zhang, D. H. Lu, X. Dai, Z. Fang *et al.*, Science **325**, 178 (2009).

[4] L. Fu and C. L. Kane, Phys. Rev. Lett. **100**, 096407 (2008).

[5] I. Garate and M. Franz, Phys. Rev. Lett. **104**, 146802 (2010).

[6] D. Pesin and A. H. MacDonald, Nat. Mater. **11**, 409 (2012).

[7] A. R. Mellnik, J. S. Lee, A. Richardella, J. L. Grab, P. J. Mintun, M. H. Fischer, A. Vaezi, A. Manchon, E.-A. Kim, N. Samarth, and D. C. Ralph, Nature (London) **511**, 449 (2014).

[8] Y. L. Chen, J.-H. Chu, J. G. Analytis, Z. K. Liu, K. Igarashi, H.-H. Kuo, X. L. Qi, S. K. Mo, R. G. Moore, D. H. Lu *et al.*, Science **329**, 659 (2010).

[9] Y. Okada, C. Dhital, W. Zhou, E. D. Huemiller, H. Lin, S. Basak, A. Bansil, Y.-B. Huang, H. Ding, Z. Wang *et al.*, Phys. Rev. Lett. **106**, 206805 (2011).

[10] L. A. Wray, S.-Y. Xu, Y. Xia, D. Hsieh, A. V. Fedorov, Y. S. Hor, R. J. Cava, A. Bansil, H. Lin, and M. Z. Hasan, Nat. Phys. **7**, 32 (2011).

[11] T. Valla, Z.-H. Pan, D. Gardner, Y. S. Lee, and S. Chu, Phys. Rev. Lett. **108**, 117601 (2012).

[12] M. R. Scholz, J. Sánchez-Barriga, D. Marchenko, A. Varykhalov, A. Volykhov, L. V. Yashina, and O. Rader, Phys. Rev. Lett. **108**, 256810 (2012).

[13] S.-Y. Xu, M. Neupane, C. Liu, D. Zhang, A. Richardella, L. A. Wray, N. Alidoust, M. Leandersson, T. Balasubramanian, J. Sánchez-Barriga *et al.*, Nat. Phys. **8**, 616 (2012).

[14] P. Sessi, F. Reis, T. Bathon, K. A. Kokh, O. E. Tereshchenko, and M. Bode, Nat. Commun. **5**, 5349 (2014).

[15] P. Roushan, J. Seo, C. V. Parker, Y. S. Hor, D. Hsieh, D. Qian, A. Richardella, M. Z. Hasan, R. J. Cava, and A. Yazdani, Nature (London) **460**, 1106 (2009).

[16] T. Zhang, P. Cheng, X. Chen, J.-F. Jia, X. Ma, K. He, L. Wang, H. Zhang, X. Dai, Z. Fang *et al.*, Phys. Rev. Lett. **103**, 266803 (2009).

[17] Y. Xia, D. Qian, D. Hsieh, L. Wray, A. Pal, H. Lin, A. Bansil, D. Grauer, Y. S. Hor, R. J. Cava *et al.*, Nat. Phys. **5**, 398 (2009).

[18] Y. Jiang, Y. Wang, M. Chen, Z. Li, C. Song, K. He, L. Wang, X. Chen, X. Ma, and Q.-K. Xue, Phys. Rev. Lett. **108**, 016401 (2012).

[19] C. Seibel, H. Bentmann, J. Braun, J. Minár, H. Maaß, K. Sakamoto, M. Arita, K. Shimada, H. Ebert, and F. Reinert, Phys. Rev. Lett. **114**, 066802 (2015).

[20] C. Pauly, C. Saunus, M. Liebmann, and M. Morgenstern, Phys. Rev. B **92**, 085140 (2015).

[21] C. Seibel, H. Maaß, H. Bentmann, J. Braun, K. Sakamoto, M. Arita, K. Shimada, J. Minár, H. Ebert, and F. Reinert, J. Electron Spectrosc. Relat. Phenom. **201**, 110 (2015).

[22] Z. Alpichshev, J. G. Analytis, J.-H. Chu, I. R. Fisher, Y. L. Chen, Z. X. Shen, A. Fang, and A. Kapitulnik, Phys. Rev. Lett. **104**, 016401 (2010).

[23] L. Fu, Phys. Rev. Lett. **103**, 266801 (2009).

[24] P. Sessi, M. M. Otrokov, T. Bathon, M. G. Vergniory, S. S. Tsirkin, K. A. Kokh, O. E. Tereshchenko, E. V. Chulkov, and M. Bode, Phys. Rev. B **88**, 161407 (2013).

[25] C.-Z. Chang, J. Zhang, X. Feng, J. Shen, Z. Zhang, M. Guo, K. Li, Y. Ou, P. Wei, L.-L. Wang *et al.*, Science **340**, 167 (2013).

[26] C.-Z. Chang, W. Zhao, D. Y. Kim, H. Zhang, B. A. Assaf, D. Heiman, S.-C. Zhang, C. Liu, M. H. W. Chan, and J. S. Moodera, Nat. Mater. **14**, 473 (2015).

[27] K. Kokh, V. Popov, A. Kokh, B. Krasin, and A. Nepomnyaschikh, J. Cryst. Growth **303**, 253 (2007).

[28] Y. Jiang, Y. Y. Sun, M. Chen, Y. Wang, Z. Li, C. Song, K. He, L. Wang, X. Chen, Q.-K. Xue *et al.*, Phys. Rev. Lett. **108**, 066809 (2012).

[29] M. F. Crommie, C. P. Lutz, and D. M. Eigler, Nature (London) **363**, 524 (1993).

[30] J. I. Pascual, G. Bihlmayer, Y. M. Koroteev, H.-P. Rust, G. Ceballos, M. Hansmann, K. Horn, E. V. Chulkov, S. Blügel, P. M. Echenique *et al.*, Phys. Rev. Lett. **93**, 196802 (2004).

[31] L. El-Kareh, P. Sessi, T. Bathon, and M. Bode, Phys. Rev. Lett. **110**, 176803 (2013).

[32] Q. Liu, X.-L. Qi, and S.-C. Zhang, Phys. Rev. B **85**, 125314 (2012).

[33] C. Pauly, G. Bihlmayer, M. Liebmann, M. Grob, A. Georgi, D. Subramaniam, M. R. Scholz, J. Sánchez-Barriga, A. Varykhalov, S. Blügel *et al.*, Phys. Rev. B **86**, 235106 (2012).

[34] P. D. C. King, R. C. Hatch, M. Bianchi, R. Ovsyannikov, C. Lupulescu, G. Landolt, B. Slomski, J. H. Dil, D. Guan, J. L. Mi *et al.*, Phys. Rev. Lett. **107**, 096802 (2011).

[35] M. Bahramy, P. King, A. de la Torre, J. Chang, M. Shi, L. Patthey, G. Balakrishnan, P. Hofmann, R. Arita, N. Nagaosa *et al.*, Nat. Commun. **3**, 1159 (2012).

[36] M. M. Yee, Z.-H. Zhu, A. Soumyanarayanan, Y. He, C.-L. Song, E. Pomjakushina, Z. Salman, A. Kanigel, K. Segawa, Y. Ando *et al.*, Phys. Rev. B **91**, 161306 (2015).

[37] H. Zhang, C.-X. Liu, X.-L. Qi, X. Dai, Z. Fang, and S.-C. Zhang, Nat. Phys. **5**, 438 (2009).

[38] M. Nagano, A. Kodama, T. Shishidou, and T. Oguchi, J. Phys.: Condens. Matter **21**, 064239 (2009).

[39] G. Bihlmayer, Y. Koroteev, P. Echenique, E. Chulkov, and S. Blügel, Surf. Sci. **600**, 3888 (2006).